Deep-Sea Research II 81–84 (2012) 114–123

Contents lists available at SciVerse ScienceDirect

Deep-Sea Research II

journal homepage: www.elsevier.com/locate/dsr2

The sources and sinks of carbon monoxide in the St. Lawrence estuarine system

Yong Zhang [a,b], Huixiang Xie [b,*]

[a] Key Laboratory of Coastal Zone Environmental Processes, Yantai Institute of Coastal Zone Research, Chinese Academy of Sciences, Yantai, Shandong Province 264003, PR China
[b] Institut des sciences de la mer de Rimouski, Université du Québec à Rimouski, Québec, Canada G5L 3A1

ARTICLE INFO

Available online 4 October 2011

Keywords:
Carbon monoxide
Photooxidation
Organic carbon cycling
Air–sea gas exchange
Estuary
St. Lawrence River

ABSTRACT

The rates of photoproduction, dark production, microbial consumption, and air–water exchange of dissolved carbon monoxide (CO) were independently assessed for the first time for a large sub-arctic estuarine water body, the Canadian St. Lawrence estuary system. Areal CO photoproduction in all four seasons increases from the Upper Estuary to the Lower Estuary to the northwestern (NW) Gulf of St. Lawrence. Areal microbial CO consumption and water-to-air flux follow the same order as photoproduction except in spring when the sequence of the Lower Estuary and the NW Gulf is reversed. Areal CO dark production tracks the ascending order of Lower Estuary < NW Gulf < Upper Estuary. Seasonally, the areal CO photoproduction and microbial CO consumption are highest in summer followed sequentially by spring, autumn, and winter. The areal CO dark production and water-to-air flux are in the ascending sequence of winter < spring < autumn < summer. Annual CO photoproduction, dark production, microbial consumption, and water-to-air flux in the St. Lawrence estuary and NW Gulf are estimated to be 4.91, 0.78, 5.45, and 0.44–0.86 Gg (gigagram) (Gg, 1 Gg = 10^9 g) CO-C, respectively. These independently estimated source (5.69 Gg CO-C yr^{-1}) and sink (5.89–6.31 Gg CO-C yr^{-1}) strengths are approximately in balance. Photoproduction accounts for 86% of the total CO source and microbial consumption takes up >86% of the total CO loss term, leaving dark production and outgassing to be the minor source and sink terms, respectively. However, the dark source is similar in magnitude to the photochemical source in the organic-rich Upper Estuary. The photochemical dissolved organic carbon (DOC) loss in the study area was elaborated using CO as a proxy of photoproduction of CO_2 and biolabile DOC.

1. Introduction

The surface ocean is almost ubiquitously oversaturated with carbon monoxide (CO) and thus releases CO to air (e.g. Conrad et al., 1982; Bates et al., 1995; Stubbins et al., 2006a) where it regulates the oxidizing capacity of the atmosphere and acts as both a direct and indirect greenhouse gas (Thompson, 1992; Evans and Puckrin, 1995). As the second most abundant inorganic carbon product (after CO_2) resulting from photooxidation of chromophoric dissolved organic matter (CDOM), CO plays a significant role in dissolved organic carbon cycling (Mopper and Kierber, 2000). Because of its high analytical sensitivity and low background concentrations, CO is arguably the most precisely measured CDOM carbon photoproduct. This has rendered CO to be used as a proxy for photoproduction of dissolved inorganic carbon (DIC) and biolabile dissolved organic carbon (Miller and Zepp, 1995; Miller et al., 2002; Stubbins et al., 2006b) and as a probe for examining the mechanisms of CDOM photochemistry (Pos et al., 1998; Stubbins et al., 2008). CO also serves as potential carbon and energy sources for certain marine microbes (King and Weber, 2007; Moran and Miller, 2007). Its short turnover times (usually <1 d) make CO an excellent tracer for modeling upper-ocean mixing dynamics (Doney et al., 1995; Kettle, 2005).

CDOM photooxidation has long been recognized as the principal CO source in surface seawater (Conrad et al., 1982). Recent evidence suggests that photodegradation of particulate organic matter (POM; Xie and Zafiriou, 2009) and thermal (dark) reactions of dissolved organic matter (DOM; Zhang et al., 2008) also significantly contribute to the seawater CO pool. CO in the water column is lost through microbial oxidation and air–sea gas exchange with the former usually being the dominant term (Conrad et al., 1982; Kettle, 2005; Johnson and Bates, 1996; Zafiriou et al., 2003, 2008). CO concentration ([CO]) in the surface ocean often exhibits strong diel variations imposed by daily fluctuations of solar insolation and fast CO removal (Conrad et al., 1982; Johnson and Bates, 1996; Zafiriou et al., 2008; Yang et al., 2010, 2011).

* Corresponding author. Tel.: +1 418 723 1986x1767; fax: +1 418 724 1842.
E-mail address: huixiang_xie@uqar.qc.ca (H. Xie).

0967-0645/$ - see front matter © 2011 Elsevier Ltd. All rights reserved.
doi:10.1016/j.dsr2.2011.09.003

During the past several decades, rates of photoproduction, microbial consumption, and air–sea exchange of CO in open oceans have been extensively investigated and thus relatively well constrained (e.g. Bates et al., 1995; Zafiriou et al., 2003, 2008; Stubbins et al., 2006a,b; Ziolkowski and Miller, 2007; Fichot and Miller, 2010). On the contrary, CO source and sink strengths are poorly understood in coastal and estuarine areas, which receive large inputs of freshwater and terrestrial organic materials and exhibit strong hydrological and biogeochemical gradients as compared to open oceans. CO studies in estuaries are particularly scarce and often focus only part of the multifaceted CO cycles. Butler et al. (1987) reported microbial oxidation rates and air–sea fluxes of CO in Yaquina Bay, Oregon. Law et al. (2002) estimated CO photoproduction and air–sea exchange rates in the Scheldt estuary, the Netherlands. Stubbins et al. (2011) measured the apparent quantum yields (AQYs) of CO photoproduction and modeled the annual CO photoproduction rate in the Tyne estuary. CO AQYs were also determined in the Mackenzie estuary (Xie et al., 2009a) and Delaware Bay (White et al., 2010) but no local CO photoproduction rates have been assessed. Therefore, none of the previous estuarine CO surveys simultaneously determined major CO production and loss rates. Furthermore, these available rates can hardly be extrapolated to other estuarine systems since estuaries often differ widely in climatic (e.g. insolation and wind speed), hydrological (e.g. tide and stratification), and biogeochemical (e.g. CDOM origin, microbial species composition and population) forcings that control CO cycling. Based partly on previously published CO AQYs and microbial CO oxidation rate constants, the present study for the first time reports independently determined photoproduction, dark production, microbial consumption, and air–sea fluxes of CO in a major sub-arctic estuarine system, the Canadian St. Lawrence estuary system. This study improves our understanding of photobiogeochemical CO cycling and the role of CDOM photooxidation in the dissolved organic carbon (DOC) cycle at land–ocean interfaces.

2. Methods

2.1. Study area

With an area of 10.8 thousand km^2 and a drainage basin of $\sim$1.3 million km^2, the St. Lawrence ranks the second largest river system in North America in terms of freshwater discharge (El-Sabh and Silverberg, 1990). The St. Lawrence estuary, stretching from Quebec City in the west to Pointe-des-Monts in the east, is customarily divided into the Upper and Lower Estuary intersected by the Saguenay Fjord (Fig. 1). The St. Lawrence estuary varies in width from 2 km at its inner limit to 24 km at the downstream limit of the Upper Estuary to 60 km at the outer limit of the Lower Estuary where it opens abruptly into the Gulf of St. Lawrence. The Upper Estuary averages only $\sim$60 m deep, sharply contrasting the deep Laurentian Channel (250–500 m deep) that extends from the head of the Lower Estuary to the eastern Canadian continental margin (El-Sabh, 1988). The turbidity maximum zone slightly downstream of the upper limit of salt intrusion is an important hydrographic characteristic in the Upper Estuary. The large size of the Lower Estuary and the Gulf results in mesoscale oceanographic features, such as upwelling near the head of the Lower Estuary, the cyclonic circulation in the northwestern (NW) Gulf, and the Gaspé current (El-Sabh, 1988; Koutitonsky and Bugden, 1991). The water column in the Upper Estuary is well mixed near its headwater but becomes partially mixed seaward (El-Sabh and Silverberg, 1990). The water column in the Lower Estuary and the Gulf is highly stratified and characterized by three distinct layers: (1) a thin ($<$50 m), seaward-flowing surface layer having a temperature of 2–10 °C and a salinity of 25–32, (2) an intermediate cold ($-$1–2 °C) and saline (31.5–33) layer, formed at the surface in winter and extending from $\sim$50 to 150 m, and (3) a warmer (3–6 °C) and saltier (34–35) landward-flowing bottom layer ($>$150 m deep) with a mixture of Labrador Current and North Atlantic waters.

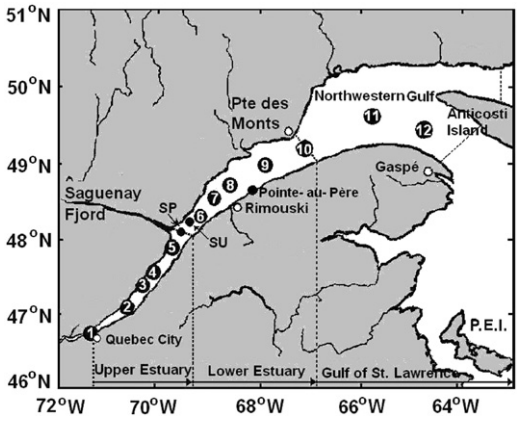

Fig. 1. Study area and sampling stations. See Table 1 for coordinates and total water depths of sampling stations.

Optically, surface water has been described as essentially CASE 1 (i.e. oceanic) water in the Gulf and CASE 2 (i.e. coastal) water in the estuary (Babin et al., 1993). Dissolved and particulate organic matters in the Upper Estuary are predominantly of terrigenous origin (Bourgoin and Tremblay, 2010). POM in the Lower Estuary and the Gulf is predominantly produced by in situ biological processes while the terrestrial signature remains noticeable in the DOM pool down there (Tremblay and Gagné, 2009). The phytoplankton primary production in the Upper Estuary is suppressed by the physical instability and high turbidity of the water column (Gobeil, 2006). Primary productivity farther downstream is higher and typically peaks in spring in the Gulf (Le Fouest et al., 2005; Mei et al., 2010) and in summer in the Lower Estuary (Therriault and Levasseur, 1985).

2.2. CO sampling and analysis

Sampling was conducted in July 2004, October 2005, December 2005, and May 2007 at stations distributed along a longitudinal transect from the upstream limit of the estuary near Quebec City to the NW Gulf (Fig. 1 and Table 1). Sampling protocols for measurements of CO AQYs (Φ_{co}), dark CO production rates (Q_{co}), and microbial CO oxidation rate constants (K_{co}) were published by Zhang et al. (2006), Zhang et al. (2008), and Xie et al. (2009b), respectively. Here we only report sampling procedures for [CO] determination. Surface water was sampled by lowering a stainless steel bucket sideways through the surface to minimize turbulence. Profile samples were taken with 12-L PVC Niskin bottles mounted on a standard conductivity–temperature–depth (CTD) rosette. Immediately after samples arrived on deck, subsamples were drawn into 50-mL metal-tipped ground-glass syringes (Perfectum®) fitted with three-way nylon valves (Kontes®). They were rinsed with sample water three times, including at least one bubble-free flushing before the final drawing. The syringes were protected against sunlight during sample transfer. Samples were analyzed as soon as they were collected. CO blanks of the sampling bottles were checked by lowering them to 300 m at station 12 in the NW Gulf and measuring [CO], assuming negligible [CO] in deep water. This yielded [CO] of 0.11 ± 0.04 nmol L^{-1} (mean $\pm$ s.d.) in summer and autumn, when no contamination-control measures were taken, and 0.05 ± 0.008 nmol L^{-1} in spring and winter, when

Table 1
Coordinates and total water depths of sampling stations in the St. Lawrence Estuarine system. Stations 1–12 were all-season stations, while station SU was sampled only in summer 2004 and SP in spring 2007. Also shown are surface areas of the three sub-regions: Upper St. Lawrence estuary (USLE), Lower St. Lawrence estuary (LSLE), and northwestern Gulf of St. Lawrence (NWG).

Region	Area[a] (10^4 km^2)	Station	Latitude (°N)	Longitude (°W)	Water depth (m)
USLE	0.35	1	46.74	71.30	56
		2	47.14	70.67	20
		3	47.28	70.54	23
		4	47.52	70.16	65
		5	47.83	69.82	76
		SP	48.12	70.62	38
LSLE	0.94	6	48.29	69.17	170
		7	48.48	69.04	325
		8	48.70	68.67	355
		9	48.92	67.97	306
		10	49.18	67.17	380
		SU	48.90	68.20	327
NWG	2.93	11	49.50	66.00	225
		12	49.40	64.75	390

[a] Areas of USLE and LSLE are from d'Anglejan (1990). Geographical extent of NWG follows the choice of Gilbert and Pettigrew (1997) and its area is calculated using ArcGIS 9.3.

the bottles were shielded from sunlight during transit between stations. The latter value was close to the instrument-plus-syringe (0.03 nmol L^{-1}). Blanks were subtracted for [CO] calculations.

[CO] was measured using a manual headspace method (Xie et al., 2002). Briefly, 5 mL CO-free air was introduced into the sample-filled 50 mL syringes (1:6 gas:water ratio). The syringe was vigorously shaken for 5 min and the equilibrated headspace air was injected into a modified trace analytical TA3000 (Trace Analytical) reduction gas analyzer for CO quantification. The system was standardized by frequent injections of a gaseous CO standard (1.23 parts per million by volume, Praxair). Precision of the [CO] measurement was estimated to be $\pm$0.02 nmol L^{-1} (or $\pm$2%). Air samples were drawn in duplicate at the bow, facing the wind, into 10-mL all-glass syringes and analyzed for CO concentration within minutes by direct injection into the CO analyzer.

2.3. Modeling CO photoproduction

Assuming negligible backscattering of light to the atmosphere, the CO photoproduction rate in the photic zone ($P_{col,co}$ in mol CO m^{-2} d^{-1}) can be modeled as follows (adapted from Zafiriou et al., 2003; Stubbins et al., 2006a; Bélanger et al., 2008):

$$P_{col,co} = \int_{280}^{600} (Q_\lambda \alpha_r R_{a,\lambda} \overline{\Phi}_{co}) d\lambda \quad (1)$$

where Q_λ (mol photons m^{-2} d^{-1} nm^{-1}) is the global spectral solar photon flux at wavelength λ under clear-sky condition, α_r is the combination of two correction factors for reflection of light by cloud (0.8) and at the air–sea interface (0.93) (Stubbins et al., 2006a), and $R_{a,\lambda}$ is the fraction of light absorbed by CDOM and particles in the photic zone (H. Xie, unpublished data), which is assumed vertically constant. Particles are assumed as efficient as CDOM at CO photoproduction (Xie and Zafiriou, 2009). $\overline{\Phi}_{co}$ (mol CO mol photons^{-1}) is the solar spectrum-weighted mean quantum yield of CDOM-based CO photoproduction, which is defined as

$$\overline{\Phi}_{co} = \frac{\int_{280}^{600} Q_{\lambda,R} \Phi_{co,\lambda}}{\int_{280}^{600} Q_{\lambda,R}}$$

where $Q_{\lambda,R}$ is the noontime cloudless spectral solar photon flux recorded in Rimouski (48.453° N, 68.511° W), Quebec, on May 24, 2005 and $\Phi_{co,\lambda}$ the experimentally determined CO spectral AQYs reported by Zhang et al. (2006). $\overline{\Phi}_{co}$ in the St. Lawrence estuarine system (SLES, defined herein as the sum of the St. Lawrence estuary and the NW Gulf) can be predicted by the following empirical equation (Zhang et al., 2006):

$$\ln(\overline{\Phi}_{co} \times 10^6) = -\frac{1626.3}{T} + 2.42 \ln(\mathrm{SUVA}_{254}) + 2.62 \quad (2)$$

T is water temperature in Kelvin and is obtained from Petrie et al. (1996) and our own cruises. SUVA_{254} is the DOC-specific UV absorption coefficient at 254 nm, which has been demonstrated to be related to the aromaticity of DOM (e.g. Weishaar et al., 2003). SUVA_{254} in our study area can be estimated as $\mathrm{SUVA}_{254} = 0.464 a_{cdom,350} + 4.09$ ($R^2 = 0.885$) where $a_{cdom,350}$ is the absorption coefficient of CDOM at 350 nm. CDOM absorption data were obtained from our own cruises (H. Xie, unpublished data). Note that Eq. (2) was established from summer samples only. The light history of CDOM is known to affect CO AQYs (Zhang et al., 2006). As the seasonal variability of the light history of CDOM in the SLES is unknown, uncertainties linked to applying Eq. (2) to other seasons are also unclear.

To estimate seasonal mean $P_{col,co}$, seasonally averaged daily global spectral photon fluxes (i.e. Q_λ in Eq. (1)) over 280–600 nm with 1 nm increments were indirectly generated from the SMARTS2 model (Gueymard, 1995, 2001). Data can be directly derived from this model are monthly averaged daily broadband (280–600 nm in our case) photon fluxes and spectral photon fluxes on mid-season days, i.e. the 15th of January, April, July, and October. We used certain approximations to calculate Q_λ. Firstly, seasonally averaged daily broadband photon fluxes were calculated from their monthly averaged counterparts. Secondly, hourly spectral photon fluxes on mid-season days were converted to both the daily broadband and spectral photon fluxes. Finally, Q_λ was obtained by multiplying the daily spectral photon flux on each mid-season day by the ratio of the seasonally averaged daily broadband photon flux in question to the daily broadband flux on that mid-season day. The inputs for the SMART2 model parameters are listed in Table A1 and the modeled Q_λ spectra are shown in Fig. 2A. The use of $\overline{\Phi}_{co}$ is justified by the fact that the relative spectral composition of the modeled Q_λ is similar to that of the solar photon fluxes used to compute $\overline{\Phi}_{co}$ in the study by Zhang et al. (2006) (Fig. 2B). Note that the relative spectral composition of the solar photon fluxes absorbed by CDOM and particles, i.e. the term $Q_\lambda R_{a,\lambda}$ in Eq. (1), does not differ substantially from that of Q_λ at λ between 280 and 510 nm but is significantly lower at longer wavelengths since $R_{a,\lambda}$ for surface waters in the SLES is typically between 0.90 and 1.0 over 280 and 510 nm but progressively more deviates from unit with further increases in wavelength ($R_{a,\lambda} = 0.40$ at 600 nm) (H. Xie, unpublished data). We evaluated that this effect underestimates $P_{col,co}$ by ca.10%, which is small as expected from the only marginal contribution of long wavelengths to $\overline{\Phi}_{co}$ (Zhang et al., 2006). Seasonal mean $P_{col,co}$, on a 91.25-d per season basis, was modeled separately for the Upper Estuary, Lower Estuary, and the NW Gulf using seasonal mean $\overline{\Phi}_{co}$ and $R_{a,\lambda}$ for each sub-region.

2.4. Dark CO production

Zhang et al. (2008) evaluated the effects of CDOM absorption ($a_{cdom,350}$ in m^{-1}), water temperature (T in Kelvin), pH, and salinity (S) on the rate of dark CO production (Q_{co} in nmol L^{-1} h^{-1}) and constructed the following empirical equation for the SLES:

$$\ln\left(\frac{Q_{co}}{a_{cdom,350}} \times 10^3\right) = -12305 T^{-1} + 0.494\mathrm{pH} - 0.0257 S + 41.9 \quad (3)$$

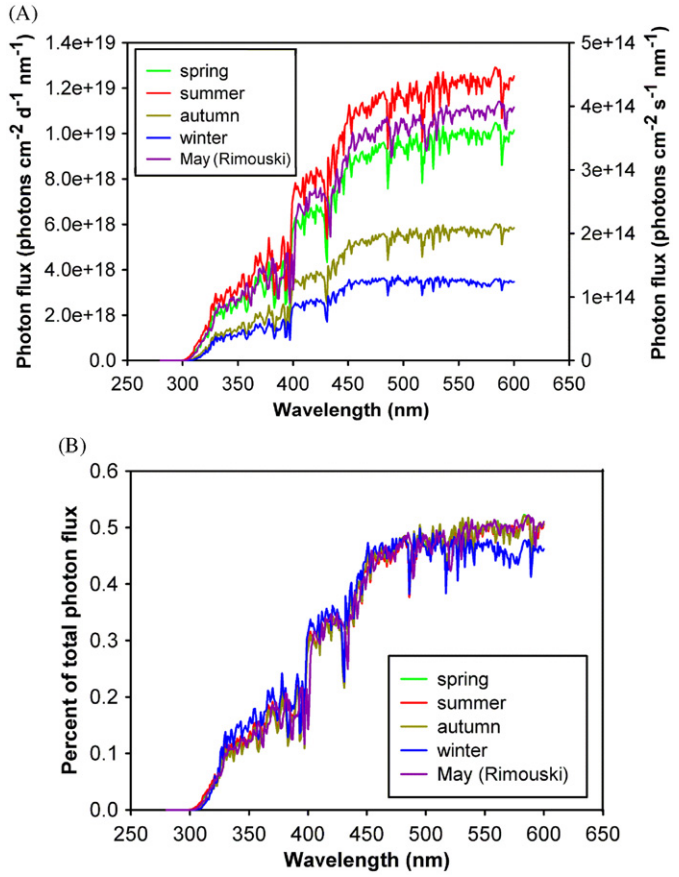

Fig. 2. (A) SMARTS2-modeled seasonally averaged daily global solar photon fluxes over the St. Lawrence estuarine region (left *y*-axis scale) and noontime cloudless solar photon flux recorded on 24 May 2005 in Rimouski, Quebec (right *y*-axis scale; Zhang et al., 2006). (B) spectral compositions of photon fluxes in (A). Total photon flux signifies photon flux integrated over the wavelength range from 250 to 600 nm.

Data of water temperature, salinity, pH, and $a_{cdom,350}$ are from Petrie et al. (1996), Lebel and Pelletier (1980), and our own cruises. The study area is divided into the same sub-regions as for the assessment of CO photoproduction. The water column of the Lower Estuary and the NW Gulf is divided into the surface mixed layer, cold intermediate layer, and bottom layer. Depths of these layers are obtained from Smith et al. (2006a,b). The Upper Estuary is regarded as a one-layer system since its water column is well mixed or only weakly stratified (El-Sabh and Silverberg, 1990). Q_{co} values $\leq 8.0\times10^{-4}$ nmol L^{-1} h^{-1} are assumed negligible; this value is the upper limit predicted for samples with undetectable CO dark production (Zhang et al., 2008). Seasonal mean Q_{co} was estimated for each depth layer of interest in each sub-region of the study area. Note that Eq. (3) was derived from 0.2 μm-filtered, stored samples. Sample storage and elimination of particles reduced CO dark production by ca. 40% and 30%, respectively (Zhang et al., 2008). These effects have been taken into account in the estimates made here.

2.5. Microbial CO consumption

Microbial CO uptake generally follows first-order kinetics year-round throughout the SLES excepting springtime in the NW Gulf when saturation kinetics prevail (Xie et al., 2009b). Consequently, all microbial CO uptake rates were calculated from first-order uptake kinetics excluding those in the NW Gulf during spring. For first-order kinetics, CO uptake rates can be quantified as $[CB]_{co}K_{co}$, where $[CB]_{co}$ is CO column burden (μmol CO m^{-2}) and K_{co} (d^{-1}) from Xie et al. (2009b). $[CB]_{co}$ was calculated by integrating CO profiles to the bottom or to a depth where [CO] was negligible. CO uptake rates were calculated for individual stations and then averaged for each sub-region of the SLES. For the autumn and winter seasons when only surface [CO] was determined, $[CB]_{co}$ was estimated by surface [CO] × 10 m, assuming that $[CB]_{co}$ equated CO inventory in a 10-m thick imaginary water layer in which [CO] was vertically homogeneous and equivalent to that at the surface. This approach overestimates $[CB]_{co}$ on average by 11% in both the spring (s.d.: 23%) and summer (s.d.: 20%) seasons when [CO] depth profiles were collected. Uncertainties associated with this approximation should be smaller for autumn and winter when vertical mixing was stronger.

2.6. Air–water CO exchange

Estimates of CO flux across the water–air interface were made using the stagnant laminar layer model of Liss and Slater (1974), which expresses the flux as a product of a transfer velocity with the difference between measured surface water [CO] and surface water [CO] in equilibrium with the atmosphere. The latter were calculated using measured atmospheric [CO] and Henry's law constants (Wiesenburg and Guinasso, 1979). Transfer velocities were calculated from wind speed parameterizations of Clark et al. (1995) for the Upper Estuary and of Wanninkhof (1992) (W-92 herein) and Liss and Merlivat (1986) (LM herein) for the Lower Estuary and NW Gulf, with CO Schmidt numbers from Zafiriou et al. (2008). The formulation of Clark et al. (1995), $K_{600}=2.0+0.24U_{10}^2$, where K_{600} is transfer velocity (cm h^{-1}) at a Schmidt number of 600 and U_{10} wind speed (m s^{-1}) at a height of 10 m, is particularly applicable to shallow estuarine water bodies and is thus most appropriate for the Upper Estuary. The positive intercept in this formulation represents enhanced gas exchange at low wind speeds due to estuarine mixing processes, such as boundary turbulence and tidal action. The Lower Estuary and NW Gulf are much wider and deeper (see Section 2.1); hence the adoption of the W-92 and LM formulations deriving from larger spatial scales. The LM formulation is more suitable to fetch-limited lake-type areas, while the W-92 parameterization applies better to fetch-unlimited oceanic environments (Wanninkhof, 1992). The W-92 relationship usually gives about twice the transfer velocities of the LM relationship. Since the Lower Estuary and NW Gulf are larger than ordinary lakes but may still be affected by wind fetch, we bracketed gas flux estimates assuming that the LM relationship yields lower limits and the W-92 relationship yields upper limits. Monthly climatological wind speeds ($1^\circ\times1^\circ$ bands), extracted from the International Comprehensive Ocean–Atmosphere Data Set (ICOADS) (2004–2007), were used to calculate seasonal fluxes for each sub-region of the study area.

3. Results and discussion

3.1. Photoproduction

Seasonal and regional CO photoproduction rates and relevant variables are shown in Table 2. Quantitatively controlled by the combination of $SUVA_{254}$ and water temperature (Eq. (2)), $\overline{\Phi}_{co}$ decreases from the Upper Estuary to the Lower Estuary to the NW Gulf in all seasons and reaches peak values in spring for the Upper Estuary and in summer for the Lower Estuary and the NW Gulf. $P_{co,col}$ exhibits the same regional pattern as $\overline{\Phi}_{co}$. Seasonally, all sub-regions show the highest $P_{co,col}$ in summer, followed sequentially by spring, autumn, and winter, in line with the seasonal trend of solar photon fluxes (Fig. 2). The area-integrated CO production, $\sum_{area}P_{co,col}$, increases from the Upper Estuary to the

Table 2
Seasonal and regional CO photoproduction rates, along with other related variables, in the St. Lawrence estuarine system. Estimates of $P_{co,col}$ and CO production are for open water only. See Table 1 for surface areas for each sub-region and for explanations of USLE, LSLE, and NWG.

Season[a]	Region	T (°C)	$SUVA_{254}$ (L mg C^{-1} m^{-1})	$\overline{\Phi}_{co}$ ($\times 10^6$)	Ice coverage[b] (%)	$P_{co,col}$ (μmol m^{-2} d^{-1})	CO production (Gg C)
Spring	USLE	4.79	6.16	3.22	11	67.52	0.23
	LSLE	1.02	4.84	1.66	10	34.69	0.32
	NWG	0.56	4.50	1.37	22	28.73	0.72
	Subtotal						1.27
Summer	USLE	12.00	5.42	2.73	0	70.86	0.27
	LSLE	5.15	4.90	1.87	0	48.44	0.50
	NWG	8.31	4.41	1.54	0	40.03	1.28
	Subtotal						2.05
Autumn	USLE	8.00	5.53	2.65	0	31.96	0.12
	LSLE	3.57	4.52	1.48	0	17.93	0.18
	NWG	7.56	4.33	1.45	0	17.46	0.56
	Subtotal						0.86
Winter	USLE	−0.30	6.14	2.86	65	22.86	0.03
	LSLE	0.13	4.93	1.70	60	13.50	0.06
	NWG	0.65	4.44	1.34	45	10.63	0.19
	Subtotal						0.28
Grand total							4.46

[a] Spring: March–May; summer: June–August; autumn: September–November; winter: December–February. Same for Tables 4–6.
[b] From the 1971–2000 Canadian Ice Service database (CIS, 2001).

Table 3
Seasonal and regional CO dark production rates, along with other related variables, in the St. Lawrence estuarine system. Only depth layers where CO dark production is detectable are listed. See Table 1 for surface areas for each sub-region and for explanations of USLE, LSLE, and NWG.

Season	Region	Depth layer (m)	T (°C)	S	pH	$a_{cdom,350}$ (m^{-1})	Q_{co}[a] (μmol m^{-2} d^{-1})	CO production[a] (Gg C)
Spring	USLE	Total (0–60)	4.79	9.75	7.76	5.04	42.19	0.12
	LSLE	Surface (0–40)	1.02	28.34	7.80	1.12	0.86	0.01
	NWG	Surface (0–40)	0.56	31.09	8.10	0.56	u.d.	u.d.
	Subtotal							0.13
Summer	USLE	Total (0–60)	12.00	9.55	7.70	3.43	88.13	0.25
	LSLE	Surface (0–30)	5.15	28.49	7.78	1.22	2.50	0.03
	NWG	Surface (0–30)	8.31	30.13	8.09	0.63	2.31	0.07
	Subtotal							0.35
Autumn	USLE	total (0–60)	8.00	9.72	7.72	3.56	48.82	0.14
	LSLE	Surface (0–60)	3.57	29.43	7.59	0.93	1.64	0.02
	NWG	Surface (0–60)	7.56	30.30	8.10	0.51	2.75	0.09
	Subtotal							0.25
Winter	USLE	Total (0–60)	−0.30	9.68	7.73	5.11	17.28	0.05
	LSLE	Surface (0–120)	0.13	30.23	7.78	0.92	0.35	0.004
	NWG	Surface (0–120)	0.65	31.21	8.07	0.41	u.d.	u.d.
	Subtotal							0.05
	Grand total							0.78

[a] Effects of storage (40%) and particles (30%) were taken into account. A blank of 8×10^{-4} nmol L^{-1} h^{-1} was subtracted (see text for explanation). u.d.: undetectable.

Lower Estuary to the NW Gulf irrespective of seasons, opposing the $P_{co,col}$ trend, due apparently to a disproportional increase in sub-region surface area from the Upper Estuary to the NW Gulf (Table 2).

The annual CO photoproduction in the St. Lawrence estuary and NW Gulf is estimated as 4.46 gigagram (Gg, 1 Gg = 10^9 g) CO-C, which increases to 4.91 Gg CO-C if a 10% underestimation due to the deviation of $R_{a,\lambda}$ from unit is added (see Section 2.3). Of this total photochemical flux, 14% is produced in the Upper Estuary, 24% in the Lower Estuary, and 62% in the NW Gulf. From a seasonal perspective, spring contributes 29%, summer 46%, autumn 19%, and winter 6% of the yearly production rate. This estimate includes CO photoproduction from both CDOM and particles (see Section 2.3). Based on the ratios of CDOM to particulate light absorption in the SLES (H. Xie, unpublished data), it is estimated that CDOM supplies ca. 80% (3.93 Gg CO-C yr^{-1}) of the total CO photoproduction with the remaining 20% (0.98 Gg CO-C yr^{-1}) from the particulate component. Note that the calculation of $\sum_{area} P_{co,col}$ assumes no CO photoproduction in water underlying ice cover, which exists during winter and early spring (Table 2). CO photoproduction in ice (Xie and Gosselin, 2005) is not taken into account owing to lack of information on this pathway in the SLES.

3.2. Dark production

Seasonal and regional CO dark production rates and relevant variables are shown in Table 3. CO dark production is detectable year-round in the entire water column of the Upper Estuary and the surface layer of the Lower Estuary. It is undetectable in all four

seasons in the subsurface layers of the Lower Estuary and NW Gulf. The surface layer of the NW Gulf has observable CO dark production only in summer and autumn. Spatially, Q_{co} always diminishes from the Upper Estuary to the Lower Estuary, conforming to the CDOM distribution in these two areas (Table 3). Q_{co} in the Lower Estuary is only slightly higher than that in the NW Gulf in summer and the direction is reversed in autumn. This evidently results from lower water temperatures and lower pH (Eq. (3)) in the Lower Estuary attributed at least partly to extensive upwelling in this region (El-Sabh, 1988). Seasonally, Q_{co} peaks in summer, followed sequentially by autumn, spring, and winter, tracking the seasonality of water temperature. The annual CO dark production amounts to 0.78 Gg CO-C in the St. Lawrence estuary and NW Gulf, of which 20% (0.16 Gg CO-C) is produced in NW Gulf, 72% (0.56 Gg CO-C) in the Upper Estuary, and only 8% (0.06 Gg CO-C) in the Lower Estuary. The much larger share by the Upper Estuary is due to its large Q_{co} as compared to the other two sub-regions.

3.3. Microbial consumption

Seasonal and regional microbial CO uptake rates, along with $[CB]_{co}$ and K_{co}, are summarized in Table 4. $[CB]_{co}$ decreases from the Upper to Lower Estuary in all seasons other than winter when the upper section is somewhat depleted in $[CB]_{co}$ relative to the lower section. $[CB]_{co}$ in the NW Gulf is higher than in the Lower Estuary in summer and autumn but the trend switches in spring and winter. Seasonally, $[CB]_{co}$ in the Upper and Lower Estuary is in descending order of summer > spring > autumn > winter, in accordance with the seasonal oscillation of solar photon fluxes (Fig. 2). The NW Gulf behaves similarly except that the sequence of spring and autumn is reversed. K_{co} decreases seaward from the Upper Estuary to the NW Gulf in all four seasons. K_{co} in all sub-regions descends from summer to autumn to winter. Spring is an exception in relation to the seasonal K_{co} progression among different sub-regions. While K_{co} in the Upper Estuary is higher in spring than in summer, K_{co} in the Lower Estuary trends inversely. Vernal microbial CO uptake in the NW Gulf is saturated and thus complies with zeroth kinetics, as noted in Section 2.5. The reader is referred to a detailed discussion of the spatio-temporal distributions and ecological implications of K_{co} given by Xie et al. (2009b). The per-unit-area CO uptake rate follows the same regional pattern as that of K_{co}. Seasonally, this quantity is at the maximum in summer followed consecutively by spring, autumn, and winter in the Upper and Lower Estuary; in the NW Gulf, however, autumn precedes spring due to the usually low vernal $[CB]_{co}$. The annual microbial CO consumption in the St. Lawrence estuary and NW Gulf is estimated to be 7.36 Gg, of which 18% is from the Upper Estuary, 32% from the Lower Estuary, and 50% from the NW Gulf. On a seasonal basis, spring contributes 19%, summer 62%, autumn 18%, and winter 1%. Note that microbial CO uptake in the water column underneath ice cover is omitted due to low [CO] in light-shielded waters (Xie and Gosselin, 2005).

The above CO uptake estimates involve potentially substantial uncertainties to which the primary contributor should be the non-random distribution of sampling time for [CO] determination. Excluding the two time-series stations, SP and SU (Fig. 1), 85% of the [CO] samples were collected between 8 a.m. and 8 p.m. and 15% between 8 p.m. and 8 a.m., Eastern Standard Time. It has been well documented that [CO] in the surface ocean displays strong diurnal variations, increasing from early morning, reaching maxima from noon to late afternoon, and decaying throughout nighttime (e.g. Zafiriou et al., 2008; Xie et al., 2009a). Law et al. (2002) reported the only time-course measurement of [CO] in an estuarine system. They found no conspicuous diurnal [CO] variability and ascribed this to more complex hydrodynamics and optical and biogeochemical characters in estuarine systems than in open oceans. To assess if diurnal [CO] variations are present in the SLES, we conducted two time-series [CO] measurements, one in summer at station SU and the second in spring at station SP (Fig. 1 and Table 1), each occupied for ca. 24 h. Results indicate that surface [CO] did show diurnal patterns but modified somewhat likely by processes such as tidal mixing, horizontal advection, and tributary freshwater runoff (Fig. 3). The 24-h mean surface [CO] is 31% lower than the mean value between 8 a.m. and 8 p.m. at stations both SU and SP. The difference is only slightly smaller (30%) in terms of $[CB]_{co}$ at station SP (no time-course $[CB]_{co}$ are available at station SU). Assuming that the overestimation in

Table 4
Seasonal and regional microbial CO uptake estimates, along with other related variables, in the St. Lawrence estuarine system. Estimates of CO uptake are for open water only. See Table 3 for ice coverage data and Table 1 for surface areas for each sub-region and for explanations of USLE, LSLE, and NWG.

Season	Region	$[CB]_{co}$ ($\mu mol\ m^{-2}$)	K_{co} (d^{-1})	CO uptake rate ($\mu mol\ m^{-2}\ d^{-1}$)	CO uptake (Gg C)
Spring	USLE	32.4	13.33	94.7	0.32
	LSLE	18.6	3.70	76.9	0.71
	NWG	9.5	0th order	14.8[a]	0.37[a]
	Subtotal				1.40
Summer	USLE	36.0	9.25	166.8	0.64
	LSLE	21.2	8.27	130.1	1.34
	NWG	40.8	2.33	79.4	2.55
	Subtotal				4.53
Autumn	USLE	21.4	8.31	84.2	0.32
	LSLE	11.5	2.62	30.8	0.32
	NWG	25.0	0.86	21.5	0.69
	Subtotal				1.33
Winter	USLE	8.8	3.14	18.3	0.02
	LSLE	10.0	0.75	7.4	0.03
	NWG	4.4	0.67	3.0	0.05
	Subtotal				0.10
	Grand total				7.36

[a] Calculated from zeroth-order uptake rates of 0.88, 0.93, and 0.55 $\mu mol\ m^{-3}\ d^{-1}$ at 2, 10, and 20 m, respectively (Xie et al., 2009b).

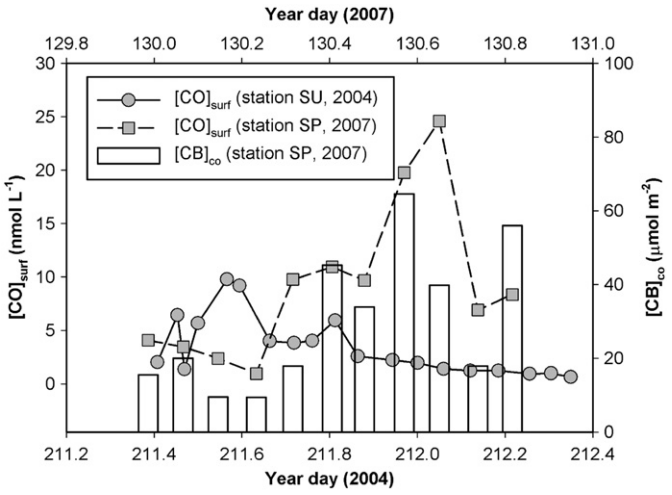

Fig. 3. Time-course surface water CO concentrations ($[CO]_{surf}$) and CO column burdens ($[CB]_{co}$) recorded at station SU in summer 2004 ($[CB]_{co}$ not available) and station SP in spring 2007.

$[CB]_{co}$ due to nonrandom sampling overall applies to samples collected between 8 a.m. and 8 p.m. throughout the St. Lawrence estuary and NW Gulf, the annual microbial CO consumption is reduced by 30% × 85%, or 26%, arriving at 5.45 Gg CO-C.

Another potential uncertainty in the estimates of microbial CO uptake rates stems from using surface water K_{co}, when K_{co} depth profiles are not available, for the whole water column. This treatment should, however, only slightly overestimate CO uptake rates since on a seasonal basis $>90\%$ of $[CB]_{co}$ resides within the surface mixed layer in which K_{co} is expected to be relatively constant (Zafiriou et al., 2003; Xie et al., 2005). The nearly absence of vertical gradients of mixed layer water temperature and heterotrophic bacterial abundance (K. Lemarchand, personal communication), which are the principal controls on K_{co} (Xie et al., 2009b), further supports a relatively invariable vertical distribution of K_{co} within the surface mixed layer.

3.4. Air–water fluxes

CO water–air fluxes, together with other relative variables, are displayed in Table 5. Surface water [CO] is year-round and ubiquitously highly over-saturated with respect to atmospheric equilibrium in the St. Lawrence estuary and NW Gulf, leading to a net flux of CO to the atmosphere. In each season other than spring, the area-integrated CO flux exhibits a consistent geographic distribution pattern, i.e. Upper Estuary < Lower Estuary < NW Gulf, in spite of variable sequences of the per unit area flux among the three sub-regions. In spring, the sequence of Lower Estuary and NW Gulf reversed. Seasonally, the areal flux is at the maximum in summer followed in descending order by autumn, spring, and winter. Neglecting CO fluxes in ice-covered waters, we estimate that there are 1.17 Gg CO-C yr^{-1} emitted from the St. Lawrence estuary and NW Gulf. Note that the flux estimates for the Lower Estuary and the NW Gulf are based on the transfer velocities derived from the W-92 formulation (see Section 2.6). If the LM formulation is adopted for these two sub-regions, the total CO flux decreases to 0.59 Gg CO-C yr^{-1}. Like the microbial CO uptake assessment, these CO flux estimates are also biased towards higher values owning to the nonrandom CO sampling pattern discussed above. Because of the extremely high saturation degrees (Table 5), the CO flux is essentially proportional to surface water [CO]. The CO fluxes are, therefore, overestimated by the same extent as that for the surface [CO], i.e. 26%. The total CO flux thus is reduced to 0.44–0.86 Gg CO-C yr^{-1} after correction for this overestimation.

3.5. Budgets of sources and sinks

CO sources and sinks in all four seasons and all three sub-regions are summarized in Fig. 4. Summing the photochemical (4.91 Gg CO-C yr^{-1}) and thermal production (0.78 CO-C yr^{-1}) arrives at a total CO source strength of 5.69 Gg CO-C yr^{-1} in the SLES. The gross dark term is 14% of the total CO production. On a sub-region basis, CO dark production corresponds to 46% of the total CO production in the Upper Estuary, 6% in the Lower Estuary, and 5% in the NW Gulf. Therefore, the contribution from the dark processes overall is small but significant. In the high-DOM Upper Estuary, the thermal and photochemical production pathways are of similarly importance in contributing to the total CO pool.

Combining the microbial consumption (5.45 CO-C yr^{-1}) with the efflux to air (0.44–0.86 Gg CO-C yr^{-1}) gives a total CO sink strength of 5.89–6.31 CO-C yr^{-1}. Microbial uptake occupies 86–92% of the total sink and the gas exchange term only accounts for 8–14%, supporting previous findings or inferences that microbial oxidation is the dominant loss term of CO in both open oceans (Zafiriou et al., 2003) and estuarine waters (Butler et al., 1987; Law et al., 2002).

The independently determined CO source (5.69 Gg CO-C yr^{-1}) and sink (5.89–6.31 CO-C yr^{-1}) strengths are thus approximately in balance for the SLES as a whole. Substantial mismatches, however, do occur for certain sub-regions and seasons (e.g. the

Table 5
Seasonal and regional CO water-to-air fluxes, along with other related variables, in the St. Lawrence estuarine system. Estimates of CO fluxes are for open water only. See Table 1 for surface areas for each sub-region and for explanations of USLE, LSLE, and NWG. Fluxes are estimated from the wind speed-transfer velocity relationships of Clark et al. (1995) for the USLE and of Wanninkhof (1992) for the LSLE and NWG.

Season[a]	Region	U_{10}[a] (m s^{-1})	k[b] (cm h^{-1})	$[CO]_{surf}$[c] (nmol L^{-1})	$[CO]_{air}$[d] (ppbv)	Saturation degree (%)	CO flux (μmol m^{-2} d^{-1})	CO flux (Gg C)
Spring	USLE	5.75	6.46	2.6	169	1191	4.07	0.014
	LSLE	6.95	12.2	5.3	117	3677	15.2	0.14
	NWG	8.13	15.4	0.84	125	543	2.54	0.064
	Subtotal							0.22
Summer	USLE	5.50	8.41	1.2	168	701	1.94	0.007
	LSLE	5.45	10.0	2.1	134	1562	5.47	0.056
	NWG	5.95	12.5	4.7	112	3750	15.1	0.48
	Subtotal							0.54
Autumn	USLE	7.22	11.3	1.7	182	805	4.14	0.016
	LSLE	7.74	15.6	1.1	120	811	3.70	0.038
	NWG	8.16	17.9	2.5	112	1856	10.2	0.32
	Subtotal							0.37
Winter	USLE	6.30	6.20	0.71	173	270	0.70	0.001
	LSLE	9.29	18.9	1.0	124	573	3.61	0.015
	NWG	9.96	22.3	0.44	116	279	1.52	0.027
	Subtotal							0.043
Grand total								1.17

[a] U_{10}: wind speed at a height of 10 m.
[b] k: transfer velocity.
[c] $[CO]_{surf}$: surface water CO concentration.
[d] $[CO]_{air}$: atmospheric CO concentration in parts per billion by volume. No $[CO]_{air}$ measurements were made in winter. Winter's values are averages of the other three seasons.

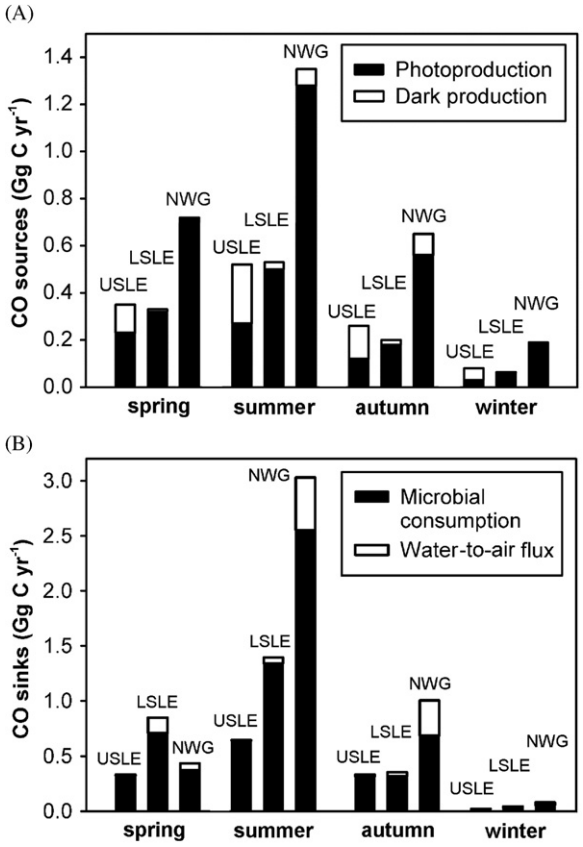

Fig. 4. Summarization of CO source and sink strengths in the study area. USLE=Upper St. Lawrence estuary; LSLE=Lower St. Lawrence estuary; NWG=northwestern Gulf of St. Lawrence.

NW Gulf region in spring and summer, Fig. 4). This inconsistency mainly arises from the fact that the corrections for the loss terms associated with nonrandom sampling often do not apply to datasets of individual sub-regions and seasons since the sampling patterns for these individual cases usually differ substantially from that for the whole dataset encompassing all sub-regions and seasons. Making suitable corrections for each sub-region and season proves difficult due to limited numbers of samples available in each sub-dataset. This underscores the importance of capturing diel cycles of [CO] in the assessment of its loss terms.

3.6. Photomineralization of dissolved organic carbon

The CDOM-based CO photoproduction in the St. Lawrence estuary and NW Gulf assessed in Section 3.1, 3.93 Gg CO-C yr^{-1}, represents 0.3% of the annual DOC influx from the St. Lawrence River (1.52 Tg C) reported by Pocklington and Tan (1987). If CO is used as a proxy for photoproduction of DIC at a mole ratio of 1 CO:20 DIC (Miller and Zepp, 1995), the estimated total photomineralization of DOC is 82.5 Gg C yr^{-1}, corresponding to 5.4% of the DOC input. Of this DOC loss, the Upper Estuary accounts for 12.0 Gg C yr^{-1}, the Lower Estuary 19.6 Gg C yr^{-1}, and the NW Gulf 50.9 Gg C yr^{-1}, equivalent to 0.8%, 1.3%, and 3.3% of the DOC input, respectively. The percent contribution combined from the Upper and Lower Estuary, 2.1%, is of the same order of magnitude as those reported for the Amazon River system, 3% on a daily basis (Amon and Benner, 1996), the Scheldt estuary, 5.5% on a daily basis (Law et al., 2002), the Mackenzie River estuary, 1–5% on a yearly basis (Bélanger et al., 2006; Osburn et al., 2009) but >10 times higher than the estimate for the Tyne estuary, 0.08–0.2% on a yearly basis (Stubbins et al., 2011). If we include the photoproduction of biolabile DOC at a molar ratio of 1 CO: 13 biolabile DOC (Miller et al., 2002), the total photochemical DOC loss in the SLES increases to 133.6 Gg C yr^{-1}, equivalent to 8.8% of the riverine DOC discharge.

It should be noted, however, that our photomineralization estimates are likely upper limits since lower ratios of DIC to CO photoproduction (5–15) have recently been observed, particularly in estuarine waters (Xie et al., 2009a; White et al., 2010). Moreover, part of the total DOC photomineralization originates from marine CDOM produced by in situ biological processes, albeit marine CDOM is considered less photoreactive than its terrestrial counterpart (Zepp, 2003; Zhang et al., 2006). Based on expected relative abundances of marine and terrestrial CDOM in different sections of the SLES, photomineralization of marine CDOM should be minor in the estuary but can be significant in the Gulf. Additionally, photochemical processes may compete with biological processes in mineralization of terrigenous DOC (Obernosterer and Benner, 2004) and may transform biodegradable DOC into bio-refractory DOC (Benner and Biddanda, 1998), thereby diminishing the net photomineralization potential.

4. Conclusions

Photooxidation predominates over thermal reactions as sources of CO in the SLES as a whole but the latter is of similar importance to the former in the organic-rich Upper Estuary. Microbial uptake prevails over gas exchange as sinks of CO throughout the SLES in all seasons. These independent estimates of CO production and loss terms are roughly in balance. CO photoproduction itself only marginally contributes to the mineralization of DOC transported downstream from the St. Lawrence River. However, the estimation of major photoproducts (i.e. CO_2 and biolabile DOC), based on CO as a proxy, suggests that photooxidation is a potentially significant terrestrial DOC removal pathway in the SLES. The primary venue where this mechanism is at play is, nevertheless, the more optically clear NW Gulf rather than the more colored estuarine section. To improve future estimates of CO source and sink strengths in the SLES requires, among the most important aspects, an evaluation of diel cycles and lateral gradients and a broader sampling coverage in the Gulf region. Higher vertical sampling resolutions also help refine these estimates.

Acknowledgments

We thank Dr. Qingshui Lu for calculating the area of NW Gulf using ArcGIS 9.3. Comments from three anonymous reviewers and the editors improved the manuscript. Yong Zhang was supported by a graduate scholarship from the Institut des sciences de la mer de Rimouski (ISMER). This work was supported by grants from the Natural Sciences and Engineering Research Council of Canada (NSERC), the Canada Foundation for Innovation (CFI), and the National Natural Science Foundation of China (NSFC, no. 41006040).

Appendix A

Inputs for the SMARTS2 model are shown in Table A1.

Table A1
Inputs for the SMARTS2 model.

Card no.	Variables	Inputs
1	Comments	Spring and summer; autumn and winter
2	Site pressure	1013.25 mb
3	Reference atmosphere	Sub-arctic summer; sub-arctic winter
4	Water vapor	Calculated from reference atmosphere and altitude
5	Ozone vertical column[a] (atm cm)	0.362 in January, 0.373 in February, 0.378 in March, 0.374 in April, 0.362 in May, 0.333 in June, 0.325 in July, 0.311 in August, 0.256 in September, 0.295 in October, 0.308 in November, 0.340 in December
6	Gaseous absorption	Pristine atmosphere
7	CO_2	370 ppmv
7[a]	Extraterrestrial spectrum	Gueymard et al. (2002) (synthetic)
8	Aerosol model	Shettle and Fenn (1979)—Maritime
9	Atmospheric turbidity[b] (AOD at 500 nm)	0.057 in January, 0.060 in February, 0.061 in March, 0.086 in April, 0.169 in May, 0.207 in June, 0.213 in July, 0.176 in August, 0.111 in September, 0.081 in October, 0.069 in November and December
10	Albedo	Seawater for spring, summer, and autumn; granular snow for winter
10[b]	Tilt Albedo	Bypass
11	Spectral range	280–600 nm
12	Output	280–600 nm, 1 nm intervals
13–16	Circumsolar/smoothing filter/illuminance/UV	Bypass
17	Solar geometry	48.5° N, 68° W; time zone: −5; time step interval: 6 min

[a] Monthly mean ozone vertical columns were obtained from the WMO World Ozone and Ultraviolet Radiation Data Center.

[b] The Level 2.0 (cloud-screened and quality-assured) monthly averaged AOD data at the Halifax site were obtained from NASA's AERONET. AOD at 500 nm is not available in November and December and the average AOD for January and October was assumed.

References

Amon, R.W.M., Benner, R., 1996. Photochemical and microbial consumption of dissolved organic carbon and dissolved oxygen in the Amazon River system. Geochim. Cosmochim. Acta 60, 1783–1792.

Babin, M., Therriault, J.-C., Legendre, L., Condal, A., 1993. Variations in the specific absorption coefficient for natural phytoplankton assemblages: impact on estimates of primary production. Limnol. Oceanogr. 38, 154–177.

Bates, T.S., Kelly, K.C., Johnson, J.E., Gammon, R.H., 1995. Regional and seasonal variations in the flux of oceanic carbon monoxide to the atmosphere. J. Geophys. Res. 100, 23093–23101.

Bélanger, S., Xie, H., Krotkov, N., Larouche, P., Vincent, W.F., Babin, M., 2006. Photomineralization of terrigenous dissolved organic matter in Arctic coastal waters from 1979 to 2003: Interannual variability and implications of climate change. Global Biogeochem. Cycles 20 GB4005.

Bélanger, S., Babin, M., Larouche, P., 2008. An empirical ocean color algorithm for estimating the contribution of chromophoric dissolved organic matter to total light absorption in optically complex waters. J. Geophys. Res. 113 (C04027).

Benner, R., Biddanda, B., 1998. Photochemical transformations of surface and deep marine dissolved organic matter: effects on bacterial growth. Limnol. Oceanogr. 43, 1373–1378.

Bourgoin, L.-H., Tremblay, L., 2010. Bacterial reworking of terrigenous and marine organic matter in estuarine water columns and sediments. Geochim. Cosmochim. Acta 74, 5593–5609.

Butler, J.H., Jones, R.D., Garber, J.H., Gordon, L.I., 1987. Seasonal distribution and turnover of reduced trace gas and hydroxylamine in Yaquina Bay, Oregon. Geochim. Cosmochim. Acta 51, 697–706.

CIS (Canadian Ice Service), 2001. Sea Ice Climatic Atlas: East Coast of Canada, 1971–2000. Canadian Government Publishing, Ottawa.

Clark, J.F., Schlosser, P., Simpson, H.J., Stute, M., Wanninkhof, R., Ho, D.T., 1995. Relationship between gas transfer velocities and wind speeds in the tidal Hudson river determined by the dual tracer technique. In: Jahne, B., Monahan, E.C. (Eds.), Air–Water Gas Transfer, AEON Verlag and Studio, Hanau, pp. 785–800.

Conrad, R., Seiler, W., Bunse, G., Giehl, H., 1982. Carbon monoxide in seawater (Atlantic Ocean). J. Geophys. Res. 87, 8839–8852.

d'Anglejan, B., 1990. Recent sediments and sediment transport processes in the St. Lawrence estuary. In: El-Sabh, M.I., Silverberg, N. (Eds.), Oceanography of a Large-scale Estuarine System, The St. Lawrence Springer-Verlag, New York, pp. 1–9.

Doney, S.C., Najjar, R.G., Stewart, S., 1995. Photochemistry, mixing and diurnal cycles in the upper ocean. J. March Res. 53, 341–369.

El-Sabh, M.I., Silverberg, N., 1990. The St. Lawrence Estuary: introduction. In: El-Sabh, M.I., Silverberg, N. (Eds.), Oceanography of a Large-Scale Estuarine System, The St. Lawrence Springer-Verlag, New York, pp. 1–9.

El-Sabh, M.I., 1988. Physical oceanography of the St. Lawrence estuary. In: Kjerfve, B. (Ed.), Hydrodynamics of Estuaries, vol. II, Estuarine Case Studies, CRC Press, Boca Raton, Florida, pp. 61–78.

Evans, W.F.J., Puckrin, E., 1995. An observation of the greenhouse radiation associated with carbon monoxide. Geophys. Res. Lett. 22, 925–928.

Fichot, C.G., Miller, W.L., 2010. An approach to quantify depth-resolved marine photochemical fluxes using remote sensing: application to carbon monoxide (CO) photoproduction. Remote Sensing Environ. 114, 1363–1377.

Gilbert, D., Pettigrew, B., 1997. Interannual variability (1948–1994) of the CIL core temperature in the Gulf of St. Lawrence. Can. J. Fish. Aquat. Sci. 54 (Suppl. 1), 57–67.

Gobeil, C., 2006. Biogeochemistry and chemical contamination in the St. Lawrence estuary. In: Wangersky, P.J. (Ed.), Handbook of Environmental Chemistry, Part H, Springer-Verlag, Berlin, pp. 121–147.

Gueymard, C., 1995. SMARTS2, a simple model of the atmospheric radiative transfer of sunshine: algorithms and performance assessment. Professional Paper FSEC-PF-270-95, Florida Solar Energy Center.

Gueymard, C., 2001. Parameterized transmittance model for direct beam and circumsolar spectral irradiance. Sol. Energy 71, 325–346.

Gueymard, C., Myers, D., Emery, K., 2002. Proposed reference irradiance spectra for solar energy systems testing. Sol. Energy 73, 443–467.

Johnson, J.E., Bates, T.S., 1996. Sources and sinks of carbon monoxide in the mixed layer of the tropical South Pacific Ocean. Global Biogeochem. Cyles 10, 347–359.

Kettle, A.J., 2005. Diurnal cycling of carbon monoxide (CO) in the upper ocean near Bermuda. Ocean Modelling 8, 337–367.

King, G.M., Weber, C.F., 2007. Distribution, diversity and ecology of aerobic CO-oxidizing bacteria. Nat. Rev. Microbiol. 5, 107–118.

Koutitonsky, V.G., Bugden, G.L., 1991. The physical oceanography of the Gulf of St. Lawrence: a review with emphasis on the synoptic variability of the motion. In: Therriault, J.-C. (Ed.), The Gulf of St. Lawrence: Small Ocean or Big Estuary? Can. Spec. Publ. Fish. Aquat. Sci., vol. 113, pp. 57–90.

Law, C.S., Sjoberg, T.N., Ling, R.D., 2002. Atmospheric emission and cycling of carbon monoxide in the Scheldt Estuary. Biogeochemistry 59, 69–94.

Lebel, J., Pelletier, E., 1980. Contribution à l'étude du pH et de la saturation en calcite dans l'estuaire du St-Laurent (Canada). Atmos. Ocean 18, 154–167.

Le Fouest, V., Zakardjian, B., Saucier, F.J., Starr, M., 2005. Seasonal versus synoptic variability in planktonic production in a high-latitude marginal sea: The Gulf of St. Lawrence (Canada). J. Geophys. Res. 110 C09012.

Liss, P.S., Merlivat, L., 1986. Air–sea exchange rates: introduction and synthesis. In: Buat-Menard, P. (Ed.), The Role of Air–Sea Exchange in Geochemical Cycling, D. Reidel, pp. 113–127.

Liss, P.S., Slater, P.G., 1974. Flux of gases across the air–sea interface. Nature 247, 181–184.

Mei, Z.-P., Saucier, F.J., Le Fouest, V., Zakardjian, B., Sennville, S., Xie, H., Starr, M., 2010. Modeling the timing of spring phytoplankton bloom and biological production of the Gulf of St. Lawrence (Canada): effects of colored dissolved organic matter and temperature. Continental Shelf Res. 30, 2027–2042.

Miller, W.L., Zepp, R.G., 1995. Photochemical production of dissolved inorganic carbon from terrestrial organic matter: significance to the oceanic organic carbon cycle. Geophys. Res. Lett. 22, 417–420.

Miller, W.L., Moran, M.A., Sheldon, W.M., Zepp, R.G., Opsahl, S., 2002. Determination of apparent quantum yield spectra for the formation of biologically labile photoproducts. Limnol. Oceanogr. 47, 343–352.

Mopper, K., Kierber, D.J., 2000. Marine photochemistry and its impact on carbon cycling. In: de Mora, S., Demers, S., Vernet, M. (Eds.), The Effects of UV Radiation in the Marine Environment, Cambridge University Press, New York, pp. 101–129.

Moran, M.A., Miller, W.L., 2007. Resourceful heterotrophs make the most of light in the coastal ocean. Nat. Rev. Microbiol. 5, 792–800.

Obernosterer, I., Benner, R., 2004. Competition between biological and photochemical processes in the mineralization of dissolved organic carbon. Limnol. Oceanogr. 49, 117–124.

Osburn, C.L., Retamal, L., Vincent, W.F., 2009. Photoreactivity of chromophoric dissolved organic matter transported by the Mackenzie River to the Beaufort Sea. Mar. Chem. 115, 10–20.

Petrie, B., Drinkwater, K., Sandström, A., Pettipas, R., Gregory, D., Gilbert, D., Sekhon, P., 1996. Temperature, salinity and sigma-t atlas for the Gulf of St. Lawrence. Can. Tech. Rep. Hydrogr. Ocean Sci. 178 V+256 pp.

Pocklington, R., Tan, F.C., 1987. Seasonal and annual variations in the organic matter contributed by the St. Lawrence River to the Gulf of St. Lawrence. Geochim. Cosmochim. Acta 51, 2579–2586.

Pos, W.H., Riemer, D.D., Zika, R.G., 1998. Carbonyl sulfide (OCS) and carbon monoxide (CO) in natural waters: evidence of a coupled production pathway. Mar. Chem. 62, 89–101.

Shettle, E.P., Fenn, R.W., 1979. Models for the aerosols of the lower atmosphere and the effects of humidity variations on their optical properties. Report AFGL-TR-79-0214, Air Force Geophysics Laboratory, Hanscom, MA.

Smith, G.C., Saucier, F.J., Straub, D., 2006a. Formation and circulation of the cold intermediate layer in the Gulf of Saint Lawrence. J. Geophys. Res. 111 C06011.
Smith, G.C., Saucier, F.J., Straub, D., 2006b. Response of the lower St. Lawrence Estuary to external forcing in winter. J. Phys. Oceanogr. 36, 1485–1501.
Stubbins, A., Law, C.S., Uher, G., Upstill-Goddard, R.C., 2011. Carbon monoxide apparent quantum yields and photoproduction in the estuary Tyne. Biogeosciences 8 (703–713), 2011.
Stubbins, A., Uher, G., Law, C.S., Mopper, K., Robinson, C., Upstill-Goddard, R.C., 2006a. Open-ocean carbon monoxide photoproduction. Deep-Sea Res. II 53, 1695–1705.
Stubbins, A., Uher, G., Kitidis, V., Law, C.S., Upstill-Goddard, R.C., Woodward, E.M.S., 2006b. The open-ocean source of atmospheric carbon monoxide. Deep-Sea Res. II 53, 1685–1694.
Stubbins, A., Hubbard, V., Uher, G., Aiken, G., Law, C.S., Upstill-Goddard, R.C., Mopper, K., 2008. Relating carbon monoxide photoproduction to dissolved organic matter functionality. Environ. Sci. Technol. 42, 3271–3276.
Therriault, J.C., Levasseur, M., 1985. Control of phytoplankton production in the Lower St. Lawrence Estuary: Light and freshwater runoff. Nat. Can. 112, 77–96.
Thompson, A.M., 1992. The oxidizing capacity of the Earth's atmosphere—probable past and future changes. Science 256, 1157–1165.
Tremblay, L., Gagné, J.-P., 2009. Organic matter distribution and reactivity in the waters of a large estuarine system. Mar. Chem. 116, 1–12.
Wanninkhof, R., 1992. Relationship between wind speed and gas exchange over the ocean. J. Geophys. Res. 97, 7373–7382.
White, E.M., Kieber, D.J., Sherrard, J., Miller, W.L., Mopper, K., 2010. Carbon dioxide and carbon monoxide photoproduction quantum yields in the Delaware Estuary. Mar. Chem. 118, 11–21.
Weishaar, J.L., Aiken, G.R., Bergamaschi, B.A., Fram, M.S., Fujii, R., Mopper, K., 2003. Evaluation of specific ultraviolet absorbance as an indicator of the chemical composition and reactivity of dissolved organic carbon. Environ. Sci. Technol. 37, 4702–4708.
Wiesenburg, D.A., Guinasso, J.N.L., 1979. Equilibrium solubilities of methane, carbon monoxide, and hydrogen in water and seawater. J. Chem. Eng. Data 24, 356–360.
Xie, H., Andrews, S.S., Martin, W.R., Miller, J., Ziolkowski, L., Taylor, C.D., Zafiriou, O.C., 2002. Validated methods for sampling monoxide and headspace analysis of carbon in seawater. Mar. Chem. 77, 93–108.
Xie, H., Gosselin, M., 2005. Photoproduction of carbon monoxide in first-year sea ice in Franklin Bay, southeastern Beaufort Sea. Geophys. Res. Lett. 32 L12606.
Xie, H., Zafiriou, O.C., 2009. Evidence for significant photochemical production of carbon monoxide by particles in coastal and oligotrophic marine waters. Geophys. Res. Lett. 36 (L23606).
Xie, H., Zafiriou, O.C., Umile, T.P., Kieber, D.J., 2005. Biological consumption of carbon monoxide in Delaware Bay, NW Atlantic and Beaufort Sea. Mar. Ecol.-Prog. Ser. 290, 1–14.
Xie, H., Bélanger, S., Demers, S., Vincent, W.F., Papakyriakou, T.N., 2009a. Photobiogeochemical cycling of carbon monoxide in the southeastern Beaufort Sea in spring and autumn. Limnol. Oceanogr. 54, 234–249.
Xie, H., Zhang, Y., Lemarchand, K., Poulin, P., 2009b. Microbial carbon monoxide uptake in the St. Lawrence estuarine system. Mar. Ecol.-Prog. Ser. 389, 17–29.
Yang, G.-P., Wang, W.-L., Lu, X.-L., Ren, C.-Y., 2010. Distribution, flux and biological consumption of carbon monoxide in the Southern Yellow Sea and the East China Sea. Mar. Chem. 122, 74–82.
Yang, G.-P., Ren, C.-Y., Lu, X.-L., Liu, C.-Y., Ding, H.-B., 2011. Distribution, flux, and photoproduction of carbon monoxide in the East China Sea and Yellow Sea in spring. J. Geophys. Res. 116 (C02001).
Zafiriou, O.C., Andrews, S.S., Wang, W., 2003. Concordant estimates of oceanic carbon monoxide source and sink processes in the Pacific yield a balanced global "blue-water" CO budget. Global Biogeochem. Cycles 17, 1015–1027.
Zafiriou, O.C., Xie, H., Nelson, N.B., Najjar, R.G., Wang, W., 2008. Diel carbon monoxide cycling in the upper Sargasso Sea near Bermuda at the onset of spring and in midsummer. Limnol. Oceanogr. 53, 835–850.
Zepp, R.G., 2003. Solar UVR and aquatic carbon, nitrogen, sulfur and metals cycles. In: Helbling, E.W., Zagarese, H. (Eds.), UV Effects in Aquatic Organisms and Ecosystems, The Royal Society of Chemistry, pp. 137–184.
Zhang, Y., Xie, H., Chen, G., 2006. Factors affecting carbon monoxide photoproduction in the St. Lawrence estuarine system (Canada). Environ. Sci. Technol. 40, 7771–7777.
Zhang, Y., Xie, H., Fichot, C.G., Chen, G., 2008. Dark production of carbon monoxide from dissolved organic matter in the St. Lawrence estuarine system: implication for global marine CO budget. J. Geophys. Res. 113 C12020.
Ziolkowski, L.A., Miller, W.L., 2007. Variability of the apparent quantum efficiency of CO photoproduction in the Gulf of Maine and Northwest Atlantic. Mar. Chem. 105, 258–270.